JGR Oceans

RESEARCH ARTICLE
10.1029/2021JC017372

On the Variability of the DWBC Transport Between 26.5°N and 16°N in an Eddy-Rich Ocean Model

Tobias Schulzki[1], Klaus Getzlaff[1], and Arne Biastoch[1,2]

[1]GEOMAR Helmholtz Centre for Ocean Research, Kiel, Germany, [2]Kiel University, Kiel, Germany

Key Points:

- Eddies and meanders cause strong temporal variability of the Deep Western Boundary Current (DWBC) flow
- Temporal variability extends the DWBC's advective timescale
- Mesoscale recirculations lead to a decorrelation of the DWBC transport at 26.5°N and 16°N

Supporting Information:

Supporting Information may be found in the online version of this article.

Correspondence to:

T. Schulzki,
tschulzki@geomar.de

Citation:

Schulzki, T., Getzlaff, K., & Biastoch, A. (2021). On the variability of the DWBC transport between 26.5°N and 16°N in an eddy-rich ocean model. *Journal of Geophysical Research: Oceans*, *126*, e2021JC017372. https://doi.org/10.1029/2021JC017372

Received 19 MAR 2021
Accepted 5 MAY 2021

Abstract The southward flow of North Atlantic Deep Water makes up the major component of the deepwater limb of the Atlantic Meridional Overturning Circulation (AMOC). In the subtropical North Atlantic, it's flow is concentrated along the continental slope, forming a coherent Deep Western Boundary Current (DWBC). Both, observations and models show a high variability of the flow in this region. Here we use an eddy-rich ocean model to show that this variability is mainly caused by eddies and meanders. Their formation process involves an important contribution from energy transfer by barotropic instability. They occur along the entire DWBC pathway and introduce several recirculation gyres that result in a decorrelation of the DWBC transport at 26.5°N and 16°N, despite the fact that a considerable mean transport of 20 Sv connects the two latitudes. Water in the DWBC at 26.5°N is partly returned northward. Because the amount of water returned depends on the DWBC transport itself, a stronger DWBC does not necessarily lead to an increased amount of water that reaches 16°N. Along the pathway to 16°N, the transport signal is altered by a broad and temporally variable transit time distribution. Thus, advection in the DWBC cannot account for coherent AMOC changes on interannual timescales seen in the model.

Plain Language Summary The Atlantic Meridional Overturning Circulation describes a northward flow of warm water close to the surface, while cold water of North Atlantic origin is transported to the south at depth. The resulting transport of heat to the north has a pronounced impact on the northern hemisphere climate and is therefore of major interest. An improved understanding of the deep flow can help to interpret past and future changes of the overturning circulation. In the subtropical North Atlantic this deep southward flow is believed to be less complex than in other regions and more confined to the western boundary. However, our results show that eddies with radii of several tens of kilometers and offshore shifts of the current impact the spreading of water. These circulation features introduce a large variety of pathways from 26.5°N to 16°N, two latitudes of long term measurements. Additionally, they cause parts of the southward transport toward 16°N to return northwards. As a result, transport changes are not propagated southward, although a strong mean flow connects the latitudes. Therefore, advection along the western boundary can not explain the modeled similarity of overturning transport changes at both latitudes.

1. Introduction

The Atlantic Meridional Overturning Circulation (AMOC) transports warm surface water northwards. It is responsible for the northward ocean heat transport with a pronounced impact on the large scale climate, especially in Europe (Srokosz & Bryden, 2015). At depth the AMOC exports cold water of North Atlantic origin (North Atlantic Deep Water; NADW) to the south, which carries anthropogenic carbon dioxide (CO_2) and other trace gases (Pickart et al., 1989; Sabine et al., 2004) away from the uptake regions in the north. A main component of the AMOC's deep limb is the Deep Western Boundary Current (DWBC; Rhein et al., 2015). While north of ~26°N interior pathways away from the western boundary were shown to exist, the flow of NADW seems to be concentrated in a coherent DWBC further south (Bower et al., 2009; Gary et al., 2011). This potentially leads to a faster spreading of tracers and trace gases in the subtropical North Atlantic (STNA). However, tracer-based velocity estimates are about one order of magnitude lower than current-meter measurements of the DWBC speed (Lee et al., 1996; Rhein et al., 2015). Observations (Kanzow et al., 2008; Lee et al., 1996) and models (Lüschow et al., 2019) suggest that the deep flow is subject to strong temporal variability associated with meanders of the DWBC and eddies. Leaman and Vertes (1996) find eddies triggered by the marked topography of San Salvador (~24°N) to reduce the mean southward

velocity of RAFOS floats compared with their speed within the DWBC itself. Mesoscale activity seems to have a strong impact on the DWBC's advective timescale, which is directly related to the southward spreading speed of temperature and salinity anomalies and the residence time of climate relevant trace gases in the deep ocean.

In addition to its importance for the transport of water masses and its properties, advection is one of three mechanisms that can cause coherent AMOC transport variability at remote sections. In modeling studies AMOC changes on interannual to decadal timescales are often found to be in phase across the STNA (e.g., Biastoch et al., 2008). In contrast to these studies, long-term AMOC measurements at the RAPID (26.5°N) and MOVE (16°N) arrays show opposing trends (Frajka-Williams et al., 2018) and interannual variations do not seem to be in phase. This raises the question on which timescale coherent changes at MOVE and RAPID may be expected and what physical drivers can cause them. Several studies suggest that boundary waves are an important driver for the propagation of AMOC signals (e.g., Getzlaff et al., 2005; Zhang, 2010). Another important process is the wind forcing, with large scale wind patterns leading to meridionally coherent AMOC changes over several degrees of latitude (Elipot et al., 2016). Although advection within the DWBC was found to be of minor importance for the coherence of variations at latitudes north of 38°N (Elipot et al., 2013), it may be different in the latitude range between 16°N and 26.5°N due to the absence of interior pathways. We do not call into question that AMOC anomalies primarily spread via wave processes in the STNA (Zhang, 2010) and that coherent variations can be caused by common wind forcing (Elipot et al., 2016). Here we want to study the missing impact of advection, which is not a trivial attempt. In a highly simplified ocean, where all water in the DWBC at 26.5°N reaches 16°N with a single transit time and constitutes all of the DWBC transport at 16°N, the correlation of the two transport timeseries would be one at the timelag corresponding to this transit time. Accordingly, under the right conditions advection can lead to highly correlated transport anomalies at remote sections. Although the real ocean is more complex, the presence of a single deepwater pathway allows to assume that deviations from these conditions are not as strong as north of 38°N.

Here we systematically assess how DWBC transport variability affects the spreading of deepwater and the coherence of transport changes at remote sections in the STNA. Our analysis is guided by the following main questions of this study:

1. How does temporal variability affect the southward spreading of deepwater in the STNA?
2. Can advection in the DWBC cause coherent AMOC changes in the STNA?

In order to address these questions, we use an an eddy-rich (1/20°) ocean model that is described and compared to observations in Section 2. Using a Lagrangian approach that is introduced in Section 3, we study volume transport pathways in the STNA and the DWBC's advective timescale (Section 4.2). Further we show how temporal variability reduces the correlation of the DWBC transport across 26.5°N and 16°N (Section 4.3) based on a purely advective view. Finally, we study physical mechanisms that drive mesoscale variability along the DWBC pathway in Section 4.4.

2. Ocean General Circulation Model

2.1. VIKING20X Configuration

In this study we use 5-day mean fields from a hindcast simulation performed with the eddy-rich ocean general circulation model configuration VIKING20X (Biastoch et al., 2021; Rieck et al., 2019). VIKING20X is a nested configuration based on the Nucleus for European Modeling of the Ocean (NEMO) version 3.6 coupled ocean/sea-ice model (Madec, 2016). The model is an expanded and improved version of VIKING20 (Böning et al., 2016). The global base model has a horizontal resolution of 0.25° on a tripolar C-grid and 46 z-levels with increasing grid spacing from 6 m at surface to 250 m at depth (ORCA025; Barnier et al., 2006). Via AGRIF two-way nesting (Debreu et al., 2008), the horizontal resolution is increased to an eddy-resolving 0.05° in the Atlantic Ocean between 70°N and 34°S. The model is forced with interannually varying air-sea fluxes derived from the CORE (version 2) data set using Bulk formulae (Large & Yeager, 2009). The model was spun-up for 30 years and then run for another 52 years covering the time period from 1958 to 2009.

2.2. Representation of the AMOC and DWBC

VIKING20X simulates a realistic overturning circulation, with a clockwise NADW cell and counter-clockwise bottom water cell (Figure S1). Consistent with observations, the maximum overturning transport is reached around 1,100 m depth (Smeed et al., 2014). The maximum AMOC transport at 26.5°N is 19.5 ± 0.6 Sv (2004–2008) compared to 18.6 ± 1 Sv derived from the RAPID array (Smeed et al., 2014). Thus, the transport falls inside the observational uncertainty expressed in terms of the standard deviation of annual means. At 16°N the modeled AMOC transport of 19.4 ± 0.8 Sv (2000–2009) exceeds the observed transport at MOVE (16.3 ± 2.6 Sv) by 3.1 Sv (Send et al., 2011).

The position, vertical structure and transport of the DWBC at 26.5°N are in good agreement with observations and other high resolution models (Bryden et al., 2005; Xu et al., 2012). The zonally averaged velocity profile within 100 km from the western boundary (Figure 1d) is comparable to estimates from Johns et al. (2005) covering a similar distance from the western boundary. In both, VIKING20X and observations, the DWBC velocity reaches its maximum at 2,000 m depth. The 1990 to 1999 mean vertically integrated southward transport of 35.7 Sv is close to mooring based estimates of 34.6 ± 3.7 Sv (Bryden et al., 2005). Also its variability is in line with previous studies. The standard deviation of the model transport is 9.7 Sv. Johns et al. (2005) report a standard deviation between 11.7 Sv (from current meters) to 14 Sv (from dynamic height moorings). Both are calculated from 40-hour low-pass filtered timeseries. Slightly higher values than our estimate based on 5-day means are therefore expected. At 16°N the DWBC transport of 29.5 Sv is also in a realistic range (25.6–28.9 Sv; Rhein et al., 2004), although long-term estimates are not published to our knowledge.

Nevertheless, there are some important differences between the modeled and observed DWBC at 26.5°N. The 10-year mean velocity exceeds 30 cm s^{-1} at individual grid points (Figure 1b). This seems high compared to mooring observations at 26.5°N indicating multi-year mean speeds of 16 cm s^{-1} (Bryden et al., 2005). Together with the realistic transport and velocity profile this suggests that the modeled DWBC is too narrow. Xu et al. (2012) and Bryden et al. (2005) find a horizontal extend of 130–160 km rather than 100 km in VIKING20X. The DWBC at 26.5°N stands out with an increased temporal variability of the flow at depth below 1,000 m (Figure 1c). In general, this agrees with the observation of strong temporal fluctuations of the DWBC strength (Kanzow et al., 2006; Lee et al., 1990, 1996), but Eddy Kinetic Energy (EKE) values are in the range of 30 cm^2 s^{-2} and therefore lower than maximum values of around 100 cm^2 s^{-2} presented by Biló and Johns (2020). Likely the mentioned discrepancies are related, as offshore meanders will increase variability, extend the mean DWBC width and reduce the mean velocity close to the western boundary. The long term mean EKE in the DWBC around 26.5°N shows a high spatial variability. Values slightly north of 26.5°N can reach up to 90 cm^2 s^{-2}. Still, such high values are too strongly confined in the vertical and to the western boundary (Figure S2). This spatial heterogeneity hints on an impact of small scale bathymetric features on the EKE within the DWBC itself. Their representation in the model could contribute to the underestimated variability at 26.5°N. Offshore variability was shown to be associated with northward propagating eddies (Biló & Johns, 2020). Such eddies are visible in the models velocity field (Movie S1), but their magnitude seems to be underestimated. At latitudes south of 24°N EKE values are in general higher and less confined to the western boundary (Figure 9d and Figure S2). Therefore, we argue that the model is able to simulate vigorous mesoscale variability in the deep STNA. It is this simulated mesoscale activity we study in the following sections. The noted differences must be kept in mind interpreting our results and are further discussed in Section 5.

3. Lagrangian Experiments

The Lagrangian analysis presented in the following sections is based on the ARIANE algorithm (Blanke & Raynaud, 1997) using the 5-day mean 3D output of VIKING20X. ARIANE solves the advection equation analytically, by assuming a stationary velocity field for 5-days. The calculation of trajectories with ARIANE using 5-day mean velocity fields is a well established method (e.g., Rühs et al., 2019). Following the argumentation of van Sebille et al. (2018) we interpret trajectories to represent pathways of small water volumes rather than single particles. Volume elements are automatically seeded along a predefined section based on the velocity field and tagged with a transport value at release. As this transport is conserved along

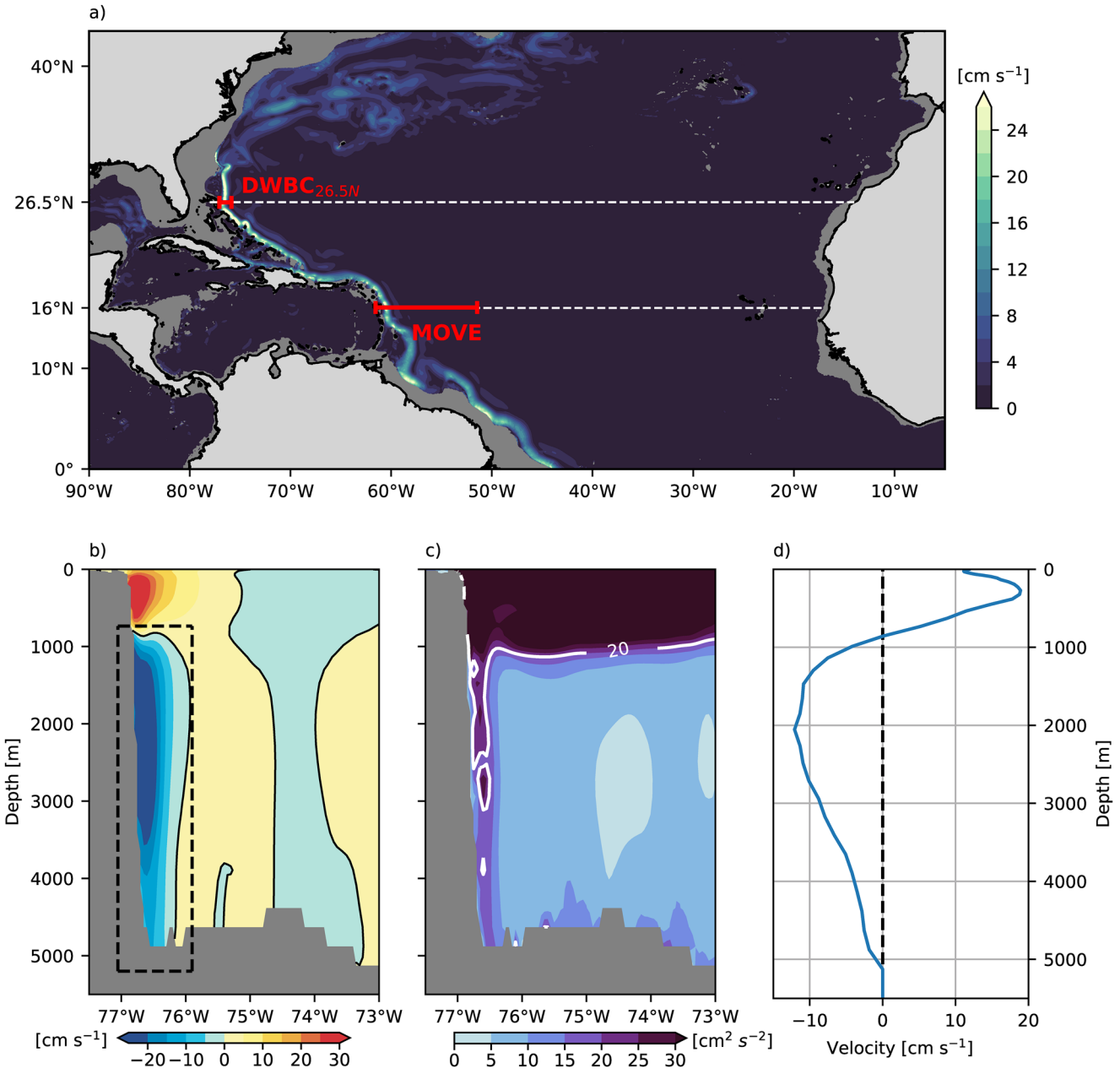

Figure 1. (a) Mean (1970–1999) speed between 1,000 and 3,500 m depth. Meridional velocity (b) and Eddy Kinetic Energy (EKE) (c) at 26.5°N. (d) Meridional velocity profile, zonally averaged within the zonal extend of the dashed box in (b). The box also indicates the ARIANE release section. Panels (b–d) show the 1990–1999 mean.

trajectories, they represent volume transport pathways. The maximum transport of a single water volume is limited to 0.1 Sv. A higher transport resolution (0.01 Sv) was tested, but does not change the results. Subsequently, ARIANE evaluates the transport across all sections of a closed domain and stores the integrated transport across all surfaces of the grid cells. This allows to obtain a two-dimensional representation of the flow field from individual trajectories by calculating the Lagrangian Stream function (LSF; Blanke et al., 1999). It is necessary to exclude the water volumes that do not exit the closed domain within the integration period. This is accomplished by restarting the ARIANE experiments with a subset of the initial release only containing water volumes that reach any section. Using the same method, it is possible to obtain the LSF of only those water volumes that reach the MOVE section or return to the release latitude.

In an initial set of experiments, water volumes were released every 5 days for each year between 1970 and 1999, resulting in 30 experiments (referred to as EXP_{var}). Here we use a zonal release section at 26.5°N, covering the longitudes from 77.05°W to 75.9°W (black line in Figure 3a) and all depth levels below 730 m. The southern boundary of the closed domain is located at 16°N and divided into multiple subsections. The MOVE section (cyan line in Figure 3a) covers the Atlantic from Guadeloupe (61.6°W) to 51.5°W. To avoid a dependence of the trajectory length on the release time step, the maximum length of all trajectories is 10 years. This experiment is thought to represent realistic conditions in the framework of the model. To assess the impact of variability, water volumes were released in the 30-year mean (1970–1999) velocity field and integrated forward in time for a maximum of 10 years in a second experiment (referred to as EXP_{mn}). This velocity field does not change throughout the entire calculation. By construction, temporal variability is excluded in EXP_{mn}. This second experiment represents a coherent DWBC, were temporally varying recirculations along the way to 16°N are excluded (see Section 4.3). The release section was chosen to fully capture the DWBC during the majority of time steps, but retain a comparable transport in the two experiments. Due to the seeding strategy of ARIANE, a too large release section would lead to a significantly increased transport in EXP_{var}. This additional transport is mostly related to Rossby waves or eddies and does not reflect an advective transport within the DWBC. The chosen release section fully contains the mean DWBC, as well as the region of highest variability (Figure 1). As a result, frequent offshore meanders that shift the DWBC out of the release box are not expected. This was verified by inspection of the 5-day mean velocity across the section. As we release particles in the variable flow field every 5 days for 30 years, a total of 2.7 million water volumes were released. EXP_{mn} is based on a single time step of the velocity field (the 30-year mean) and therefore water volumes are released at one time step only. This results in a lower number (700) of released water volumes.

The previously described experiments only trace water that originates from 26.5°N. We run a third experiment to test, if other sources of the DWBC at 16°N exist (referred to as EXP_{16N}). Therefore we release water volumes along a zonal section at 16°N (61.5°W–59.7°W). The width of this section is chosen to capture 90% of the transport arriving from 26.5°N in EXP_{var}. Again we release water volumes every 5 days for each year between 1970 and 1999, resulting in a total release of 2.4 million water volumes. As for EXP_{mn} and EXP_{var}, the integration is limited to 10 years and the boundaries of the closed domain are unchanged. However, we track water volumes backward in time to find their source region.

The three experiments were specifically designed to answer our main questions introduced in Section 1. While EXP_{var} alone is used to estimate the timescale and pathways of the DWBC in the STNA, a comparison with EXP_{mn} reveals the impact of temporal variability on the transit time distribution (TTD). These two forward experiments capture the flow of water transported in the DWBC at 26.5°N, but most likely not all water volumes that contribute to the DWBC at 16°N. EXP_{16N} allows to study the impact of other sources on the DWBC's variability at 16°N.

In order to further disentangle the impact of the TTD on the correlation of transport signals at different latitudes, we set up an idealized experiment using the PARCELS software package (Delandmeter & van Sebille, 2019). Here our attempt is not to reproduce realistic pathways, but to study the impact of different TTDs. Therefore we release particles at 39 discrete points along a section that represents 26.5°N for 2,190 time steps. This corresponds to a release every 5 days from 1970 to 1999. These particles are then advected purely in meridional direction until they reach a distant section. The velocity at each grid point is set to a certain value that is kept constant along the entire way to the southern boundary. Therefore, the release grid point is tied to a specific transit time from the release to the distant section. We define these transit times to match the bin centers of the TTD shown in Figure 3. By changing the number of particles released per grid point at different time steps, we can simulate a release timeseries. Here we simulate the DWBC transport timeseries at 26.5°N. Further it is possible to scale the number of released particles depending on their release grid point, or equivalently, depending on their transit time. This allows to simulate different TTDs and study their impact on the correlation between the timeseries of released particles and particles arriving at the distant section.

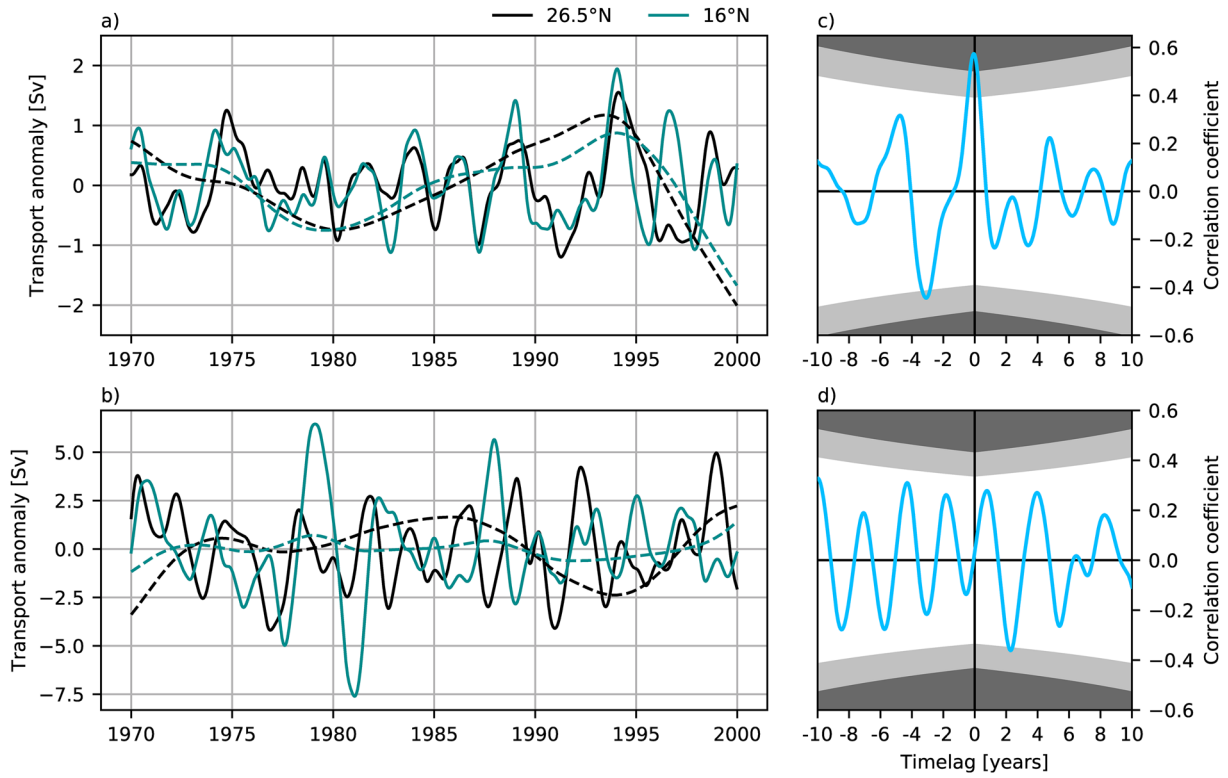

Figure 2. Low-pass filtered timeseries of the Atlantic Meridional Overturning Circulation (AMOC) (a) and Deep Western Boundary Current (DWBC) transports (b) at 26.5°N and 16°N. Solid (dashed) lines show interannual (decadal) anomalies. Cross-correlation of the interannual AMOC (c) and DWBC (d) timeseries at 26.5°N and 16°N. Gray shaded areas indicate significant correlation coefficients based on a confidence level of 95% and 99%. 26.5°N leads at positive lags.

4. Results

4.1. AMOC and DWBC Correlation

In agreement with studies by Biastoch et al. (2008) and Bingham et al. (2007) the AMOC at 26.5°N and 16°N shows coherent variability on interannual and decadal timescales (Figure 2). We define decadal changes as variations of the low-pass filtered timeseries, using a second-order butterworth filter with a cut-off frequency of 119 month. Interannual changes are studied using the 23-month low-pass filtered timeseries with the decadal signal subtracted. Before further analysis, we exclude half of the filtering period at the beginning and end and detrend the timeseries. Statistical significance is derived from a student t-test, where the effective degrees of freedom are calculated according to Emery and Thomson (2001). The correlation of the interannually filtered AMOC timeseries is significant based on a confidence level of 99% with 0.57. The maximum correlation is not exactly reached at timelag zero, but with 16°N leading by one month. Nevertheless, we describe the correlation to be instantaneous in the following. Also variations on decadal timescales are in phase with a significant instantaneous correlation of 0.95. In contrast to the AMOC, the correlation of the DWBC is strongly reduced on both timescales. The correlation does not exceed 0.33 for the interannual timeseries and is not statistically significant on the 95% level (Figure 2d). The DWBC correlation is higher with 0.76 on the decadal timescale and significant on the 95% confidence level. Here we define the DWBC transport as the southward transport across fixed boxes. These boxes correspond to the ARIANE release sections. To ensure that the lack of correlation is not just caused by the DWBC meandering to more offshore positions, we repeat the analysis defining the DWBC as the minimum of the cumulative transport below 1,000 m (Figure S3). Also with this alternative definition, there are no peaks in the cross-correlation that could be explained by advection. Additional to the lack of coherent variability in the DWBC, we find a 3–4 times enhanced interannual standard deviation of the DWBC transport compared to the AMOC.

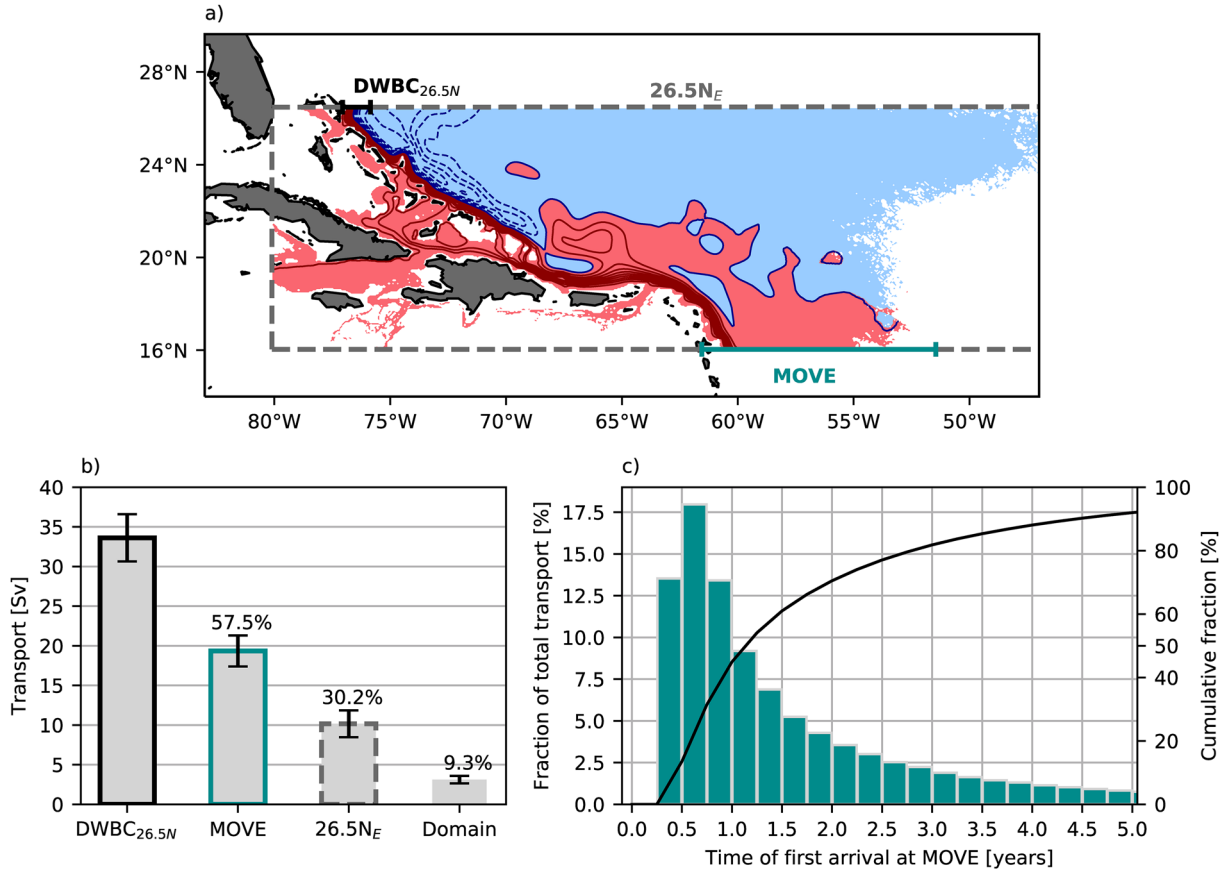

Figure 3. (a) Lagrangian Stream function (LSF) of all water volumes released in EXP_{var}. Contours are drawn with an interval of 2 Sv. The release section is colored black and the MOVE section cyan. All other sections of the closed domain are shown as dashed gray lines. (b) Transport across the boundaries of the closed domain. The mean transport of all 30 release years is shown together with the ensemble standard deviation (error bars). The transport fraction in % of the total release ($DWBC_{26.5N}$) is annotated. Domain refers to the transport that does not cross any section within 10 years after the release. (c) Transit time distribution (TTD) of the transport to MOVE. The line shows the cumulative fraction of the transport. The transport that has arrived after 10 years is defined as 100%.

Although previous studies find the flow of NADW to be concentrated in a narrow band along the western boundary, which is supported by the modeled velocity structure (Figure 1a), there is apparently no impact of this advection on the coherence of changes at both latitudes. This is true for the net transport across the whole Atlantic (the AMOC) and even for the southward transport close to the western boundary (the DWBC). In the following we test three hypothesis that could explain this observation:

1. There is no continuous pathway of NADW that connects both latitudes.
2. The timescale of advection in the DWBC is so long, that it's impact can not be seen in the 30-year long timeseries analyzed here.
3. The transport signal considerably changes between the latitudes of 26.5°N and 16°N.

4.2. Advective Pathways and Timescale

An average transport of 33.6 Sv per time step are released in EXP_{var} and subsequently advected in the full 5-day mean velocity field for 10 years. More than half of this transport (19.3 Sv) reaches 16°N (Figure 3b). The LSF shows that the majority of this transport follows the western boundary (Figure 3a). Interior southward pathways fed by the DWBC are not visible and all of the transport that reaches the southern domain boundary crosses 16°N close to the western boundary. These results already allow to falsify the first hypothesis, as a continuous DWBC is clearly existent in the model. Nevertheless, not all of the released transport reaches the MOVE latitude. A significant fraction of the transport released in the DWBC at 26.5°N is

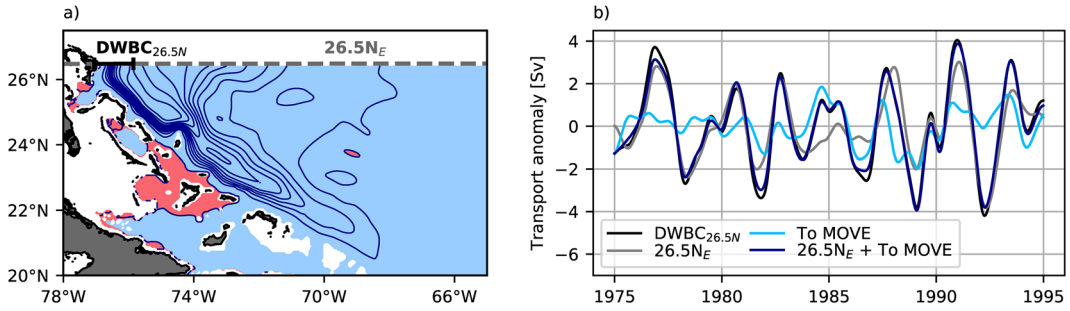

Figure 4. (a) Lagrangian Stream function (LSF) of only those water volumes that return to 26.5°N in EXP_{var}. Contours are drawn with an interval of 1 Sv. (b) Interannually filtered transport anomalies. $DWBC_{26.5N}$ (black) refers to the southward transport across the release section and equals the Eulerian definition of the Deep Western Boundary Current (DWBC). "To MOVE" (light blue) denotes the transport that ultimately reaches the MOVE section and $26.5N_E$ (gray) the transport that returns to the release latitude. The sum of both is shown in dark blue.

returned to the release latitude (30.2% or 10.2 Sv). Another 3.1 Sv do not reach any section of the closed domain within 10 years after the release. Additional analysis (not shown) shows that these water volumes are detrained from the DWBC and then trapped inside a closed circulation within the ocean interior. A small fraction of the transport enters the Caribbean Sea through the Windward and Anegada passages.

The fastest water volumes to reach the MOVE section need 96 days for the ~2,360 km long pathway along the western boundary. This corresponds to a velocity of nearly 30 cm s^{-1}, in line with Eulerian velocities in the DWBC core. The full TTD (Figure 3c) has a modal value between 0.5 and 0.75 years. The mean (1.9 years) and median (1.1 years) transit times are both well below 2 years. Accordingly, the mean southward spreading velocity of water that is advected from 26.5°N to 16°N is 4 cm s^{-1}. This is within the range of estimates directly derived from tracer observations (2.5 cm s^{-1}; Rhein et al., 2015) and theoretical models used to explain the observed tracer distributions (about 5 cm s^{-1}; Rhein, 1994; Waugh & Hall, 2005). Since the advective timescale is below 2 years, hypothesis 2 is not able to explain the lack of correlation in the DWBC transport at both latitudes.

4.3. Decorrelation of the Transport Timeseries

As hypotheses 1 and 2 are not able to explain the lack of correlation in the DWBC, we are now investigating how the transport timeseries is changed along the pathway to 16°N. As explained in the introduction, in a highly simplified ocean where the TTD can be approximated by a single peak, the maximum lagged cross-correlation would be one. In the real ocean however, deviations from these assumptions decrease the maximum cross-correlation. Here we follow the path of water transported in the DWBC from 26.5°N to 16°N and show three different mechanisms that ultimately result in an insignificant correlation of the DWBC transport timeseries at 16°N and 26.5°N on interannual timescales. At the same time we will investigate how the same mechanisms increase the DWBC's advective timescale, contributing to the spread between tracer and current-meter estimates.

4.3.1. Recirculation to 26.5°N

As already noted, not all of the transport released in the DWBC does reach the MOVE section. The return flow partly arises from a cyclonic recirculation north of San Salvador (24°N) and partly from mesoscale recirculation gyres seen along the DWBC pathway further south (Figure 4a).

Using ARIANE it is possible to split the timeseries of the DWBC at 26.5°N into individual transport timeseries based on the section where this transport leaves the closed domain (Figure 4b). Due to the seeding strategy in ARIANE, at any given time step the sum of all water volumes released equals the DWBC transport when defined as the southward transport across the release box. The interannual variability of the DWBC at 26.5°N is entirely explained by the combination of the timeseries reaching MOVE and the recirculating transport. The correlation between the sum of both timeseries (dark blue line) and the Eulerian DWBC timeseries (black line) is 0.99. Although the mean flow is dominated by water volumes that reach

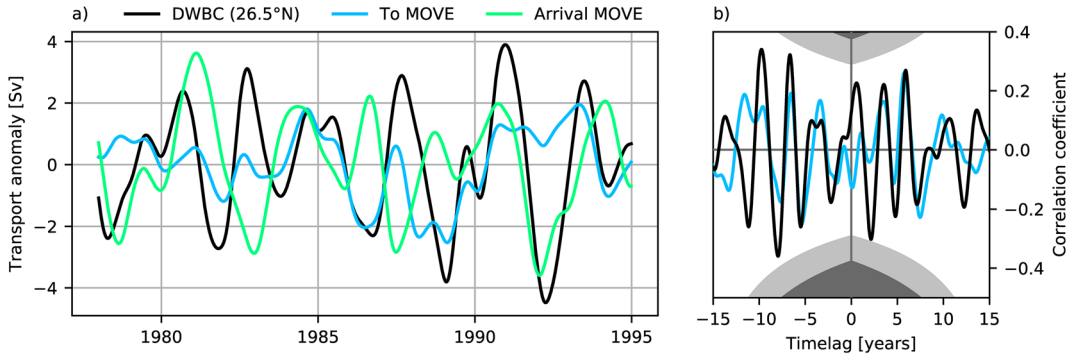

Figure 5. (a) Interannually filtered timeseries of the Eulerian Deep Western Boundary Current (DWBC) transport at 26.5°N and transport components derived from EXP_{var}. "To MOVE" denotes the transport of water volumes that ultimately reach 16°N sampled at the release section. "Arrival MOVE" shows the timeseries of the same water volumes, but sampled at arrival at 16°N. (b) Cross-correlation of the "Arrival MOVE" and "To MOVE" timeseries (blue), as well as "Arrival MOVE" and DWBC (26.5°N) timeseries (black). Timeseries showing a transport at 26.5°N lead at positive lags.

16°N, this is not true for the interannual variability. The flow to MOVE (light blue line) contributes about 20 Sv to the mean DWBC transport at this latitude and thus about twice as much as the recirculation to the $26.5N_E$ section (gray line). Nevertheless, the contribution to the interannual variability is larger for the recirculation component. Comparing the standard deviation, the recirculation (1.5 Sv) is more variable than the transport to 16°N (0.8 Sv). Also the correlation with the Eulerian DWBC is higher for the recirculation with a correlation coefficient of 0.9 compared to 0.55.

Although most of the water volumes that are released in the DWBC at 26.5°N reach 16°N, additional water volumes that are associated with an above average transport mostly return to the release section.

4.3.2. Variable pathway to 16°N

According to Section 4.2 water volumes are not advected to 16°N with a single transit time, but can take various different pathways that result in a rather broad distribution. Here we systematically assess how and why the transport signal changes from the release at 26.5°N to the arrival at 16°N.

To compare the two signals, at each time step we sample the transport of all water volumes when released at 26.5°N ("To MOVE") and during their arrival at 16°N ("Arrival MOVE"). Note that we exclude the first 3 years of the timeseries to allow a sufficient amount of water from the first release time steps to reach 16°N. In contrast to an idealized DWBC with a single transit time, the interannual transport signal is strongly changed along the pathway to 16°N (Figure 5a). As the advection of the signal is connected to a timelag, we do not expect a high instantaneous correlation and therefore calculate the cross-correlation (Figure 5b). The maximum cross-correlation at lags consistent with the TTD (between 1 and 2 years) is smaller than 0.2. Slightly higher values can be seen for longer timelags, but none of them are statistically significant different from zero. Consistently, there is also no significant correlation of the DWBC at 26.5°N and the transport arriving at MOVE. This change of the signal along the pathway therefore strongly contributes to the decorrelation of the interannual DWBC transport changes at 26.5°N and 16°N. It reduces the maximum cross-correlation from 0.55 (see previous section) to insignificant values below 0.2.

After showing its importance for the transport timeseries, we now study what causes the TTD to deviate from a single peak. By comparing the release experiment using a variable velocity field (EXP_{var}) to a release in the climatological mean velocity field (EXP_{mn}), it is possible to derive the impact of temporal variability. The released transport in both experiments differs by less than 1 Sv, verifying an appropriate choice of the release section. The transport that reaches MOVE is about 3 Sv higher in EXP_{mn}, which is mainly compensated by a weaker return flow to 26.5°N. In both experiments the water volumes follow the DWBC along the shelf break (Figures 6a and 6b). However, in EXP_{mn} recirculations along the pathway are largely excluded, especially west of 68°W. Between 68°W and 60°W water volumes follow an anticyclonic meander in both experiments. Nevertheless, this meander is stronger and has a more complex structure in EXP_{var}. Overall,

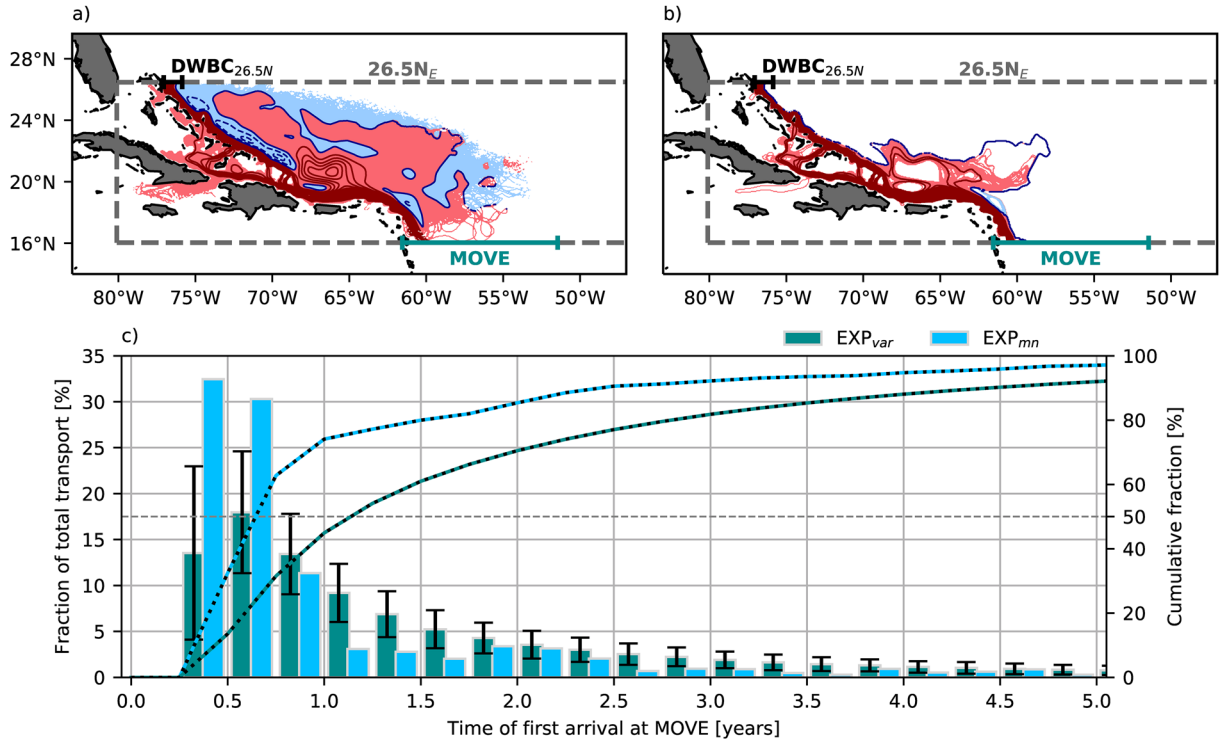

Figure 6. Lagrangian Stream function (LSF) of only those water volumes that reach the MOVE section in EXP_{var} (a) and EXP_{mn} (b). Contours are drawn with an interval of 1 Sv. (c) Transit time distribution (TTD) of the transport to MOVE from EXP_{mn} and EXP_{var} (as Figure 3c). Error bars show the standard deviation from calculating the TTD for each release time step in EXP_{var} individually.

we conclude that temporal variability introduces a variety of different pathways from 26.5°N to 16°N by allowing water volumes to follow recirculations but still reach the MOVE section. Note that the LSF of all water volumes is similar in EXP_{mn} (Figure S4) and EXP_{var}. However, in EXP_{mn} nearly all water volumes that follow these recirculations are returned to 26.5°N. Therefore we can use EXP_{mn} as a representation of a flow without recirculations along the way to 16°N. Estimated differences should be interpreted as a lower limit because not all recirculations are fully excluded.

The larger variety of pathways in EXP_{var} is also connected to a larger variety of transit times resulting in a broader TTD (Figure 6c). Especially, the advective peak is largely reduced in EXP_{var}. In EXP_{mn}, more than 30% of the total transport reaches the MOVE section between 0.25 and 0.5 years after the release More than 60% do so within the first 0.75 years and thus twice as much as in EXP_{var}. The more gradual increase of the cumulative distribution further illustrates the shift to longer transit times when temporal variability is considered. Along with the reduction of the advective peak the median (mean) of the distribution is shifted by 0.3 (0.4) years due to temporal variability of the flow. In contrast, the minimum transit time to reach the MOVE section is 10 days shorter in EXP_{var}. This is likely explained by water volumes that continuously follow the DWBC when it is stronger than average. Another important result is that even without temporal variability, the TTD can not be approximated by a single peak. Partly because the anticyclonic meander between 68°W and 60°W is not fully excluded and secondary pathways along the coast of Cuba and Puerto Rico exist. The more import reason, however, is the nonuniform velocity structure of the DWBC itself. The velocity is largest in a well defined core of the DWBC and gradually decreases away from the western boundary. The strong deviation of the real TTD from a single peak and the spread between tracer and current-meter estimates can be explained by two mechanisms. A nonuniform velocity structure of the DWBC and mesoscale recirculation gyres.

In a last step we combine the previous results of this section and show how different TTDs change the correlation of an advective signal at remote locations by studying idealized experiments (Section 3). The "To MOVE" timeseries (Figure 5a) is used to release particles along a section, which are then sampled at a

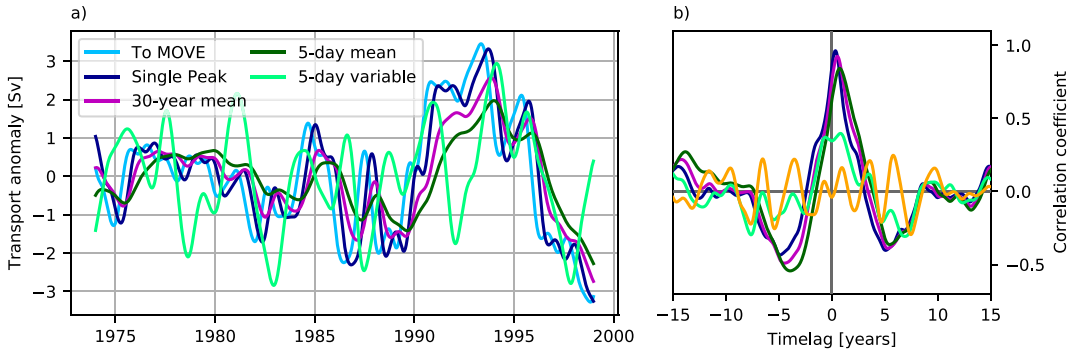

Figure 7. (a) 23-month low-pass filtered timeseries (decadal signal included) of the transport to MOVE (see Section 4.3) and the transport arriving at MOVE in idealized experiments with different transit time distributions (TTD). "Single Peak" refers to an experiment with a single transit time of 136 days. "30-year mean" and "5-day mean" are run with the TTDs shown in Figure 6. In "5-day variable" the TTD is derived from every release time step of EXP_{var} individually and therefore changes with time. (b) Cross-correlation of the timeseries (same color coding as in left panel) with the "To Move" timeseries. The orange line shows cross-correlation of "5-day variable" and "To Move", but with the decadal signal removed.

remote section, similar to our analysis of the ARIANE experiment. However, we do not exclude the decadal signal in this case, to also study the effect of different TTDs on this timescale. As expected, the signal is not changed when the TTD has a single peak (Figure 7). Release and arrival are cross-correlated with a maximum of 0.96 at the lag approximately corresponding to the transit time between the sections (136 days). The cross-correlation is not exactly 1 for two reasons. First, excluding the first three years is reasonable based on the TTD, but not enough to allow all water volumes from the first release time steps to reach the remote section. Second, the timelag is larger than 0 and therefore the cross-correlation is influenced by the zero-padding at the beginning and end of the timeseries. This is necessary because our timeseries are of finite length. Considering the DWBC's velocity structure by applying the TTD derived from EXP_{mn} reduces the correlation to 0.92 at a timelag of 185 days. The correlation is further decreased by adding the mean effect of temporal variability. For that we apply the TTD shown in Figure 3c derived from EXP_{var}. Even with the broader TTD, the maximum cross-correlation is still 0.84 at a timelag of 265 days. As the TTD gets broader, the correlation is only slightly reduced, but the maximum correlation is shifted to a longer lag time. The correlation drops to 0.4 at timelag 290 days, when it is also considered that the TTD itself is not constant, but depends on the release time step (see error bars in Figure 6c). Here the timelag is similar because the mean TTD is still the same, but the correlation is strongly reduced compared to the experiment with a broader TTD alone. Further, most of this correlation is caused by low frequency variability. Removing the decadal signal (119-month low-pass filtered), as for the ARIANE experiments, reduces the correlation from 0.4 to values below 0.25. The latter correlation is not statistically significant. Overall, this experiment is able to reproduce the timeseries at arrival in ARIANE to a large extend (correlation 0.99 with the decadal signal removed), despite its high simplicity. While the interannual signal is strongly altered along the pathway, the decadal signal is nearly unchanged by advection. This suggests that the change of the transport signal along the pathway is dependent on the timescale and almost negligible for decadal changes. However, our 30-year long timeseries is not long enough to make robust statements on this timescale.

Another interesting observation is the change of the signals amplitude (or its variability). A broad TTD causes the signal to be spread over a range of timescales, attenuating its amplitude. The releases using a temporally constant TTD show a lower variability of the arriving signal compared to the released signal. However, if the TTD depends on the release time step, the variability of the arriving signal is amplified. This matches the ARIANE experiment (Figure 5), where the arriving signal has a higher standard deviation.

4.3.3. Recirculation across 16°N

Integrating trajectories released in the DWBC at 16°N backwards in time (EXP_{16N}) reveals that not all these trajectories originate from 26.5°N (Figure 8). In agreement with the forward experiment (EXP_{var}) about 18 Sv of the DWBC at 16°N arise from a southward flow along the western boundary. This flow accounts for 61.2% of the DWBC transport across the MOVE section. Note that the "From 26.5°N" timeseries derived

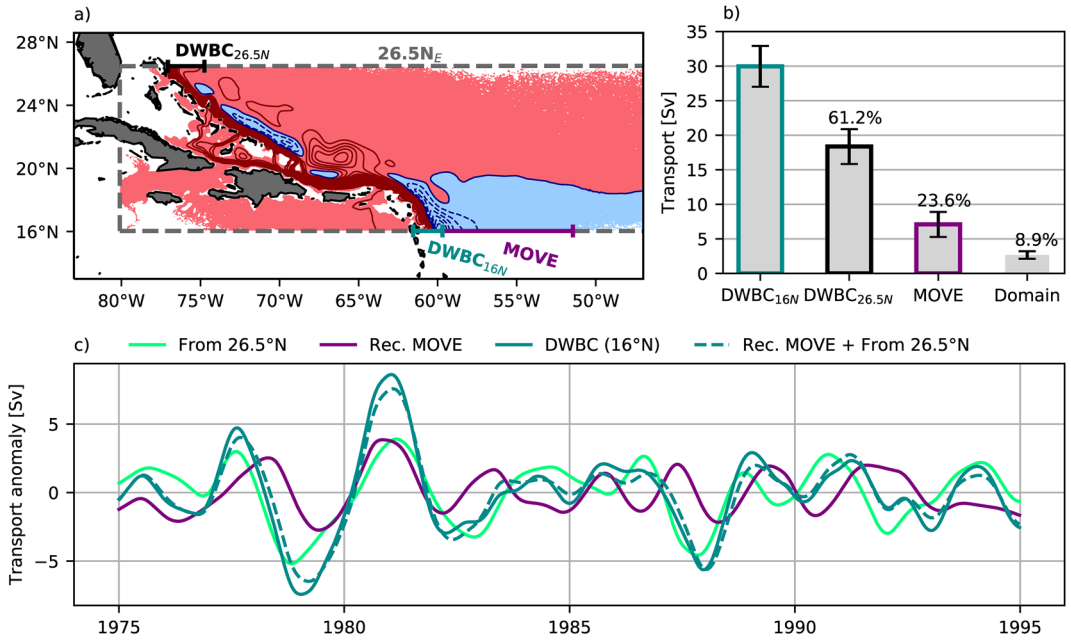

Figure 8. (a) Lagrangian Stream function (LSF) of all water volumes released in EXP_{16N} (backward tracking). Contours are drawn with an interval of 1 Sv. The release section ($DWBC_{16N}$) is shown in cyan. (b) Transport across the boundaries of the closed domain. The mean transport of all 30 release years is shown together with the ensemble standard deviation (error bars). Domain refers to the transport that does not cross any section within 10 years after the release. The transport fraction in % of the total release ($DWBC_{16N}$) is annotated. (c) Timeseries of the interannually filtered transport arriving at the release section in EXP_{16N} from the $DWBC_{26.5N}$ and MOVE sections. Additionally the sum of both is shown along with the Eulerian DWBC transport at 16°N.

from the backward experiment and the "Arrival MOVE" timeseries derived from the forward experiment (Figure 5) are closely related (correlation: 0.91) and represent the same water volumes. A nonnegligible contribution of 7 Sv is added by water that crosses 16°N in northward direction. This water is mostly entrained into the DWBC south of 20°N. These two components explain the majority of interannual variations of the DWBC at 16°N, as indicated by the similarity of the dashed and solid cyan lines in Figure 8. In contrast to 26.5°N, the recirculation component seems to be less dominant in controlling the DWBC's interannual variations. The recirculation component is slightly less variable than the transport from 26.5°N on interannual timescales and its correlation with the DWBC is lower (0.52 for the recirculation and 0.85 for the transport arriving from 26.5°N). A summary of all mentioned correlations related to the ARIANE experiments is provided in Table S1. The timeseries of the transport that arrives from 26.5°N is already not significantly correlated with the DWBC at 26.5°N (Section 4.3). Additionally, this transport does not fully provide the DWBC transport at 16°N. This can explain the lack of statistically significant peaks in the cross-correlation of the DWBC timeseries at 16°N and 26.5°N (Section 4.1).

4.4. Drivers of Mesoscale Recirculations

In the previous section we highlighted the importance of mesoscale recirculation gyres along the DWBC in the STNA. Therefore, we now turn our attention to the mechanisms driving these recirculations. Because the recirculations are visible in EXP_{mn}, they are present in the 30-year averaged flow field. Nevertheless, they are not caused by a steady flow following the bathymetry. The flow adjacent to the DWBC is highly variable (Movie S1). This is further illustrated by Hovmöller plots of the meridional velocity anomaly at 26.5°N, 20°N and 16°N (Figure 9). At all latitudes the flow in the interior ocean is characterized by anomalies propagating westward with ~ 4 cm s^{-1} (depending on the latitude). This speed is in agreement with the phase speed of first mode baroclinic Rossby waves in this latitude range (Gill, 1982). Close to the western boundary, velocity anomalies show a higher magnitude and have distinct characteristics. At 20°N the flow west of 60°W is characterized by northward anomalies that go along with southward anomalies to their east,

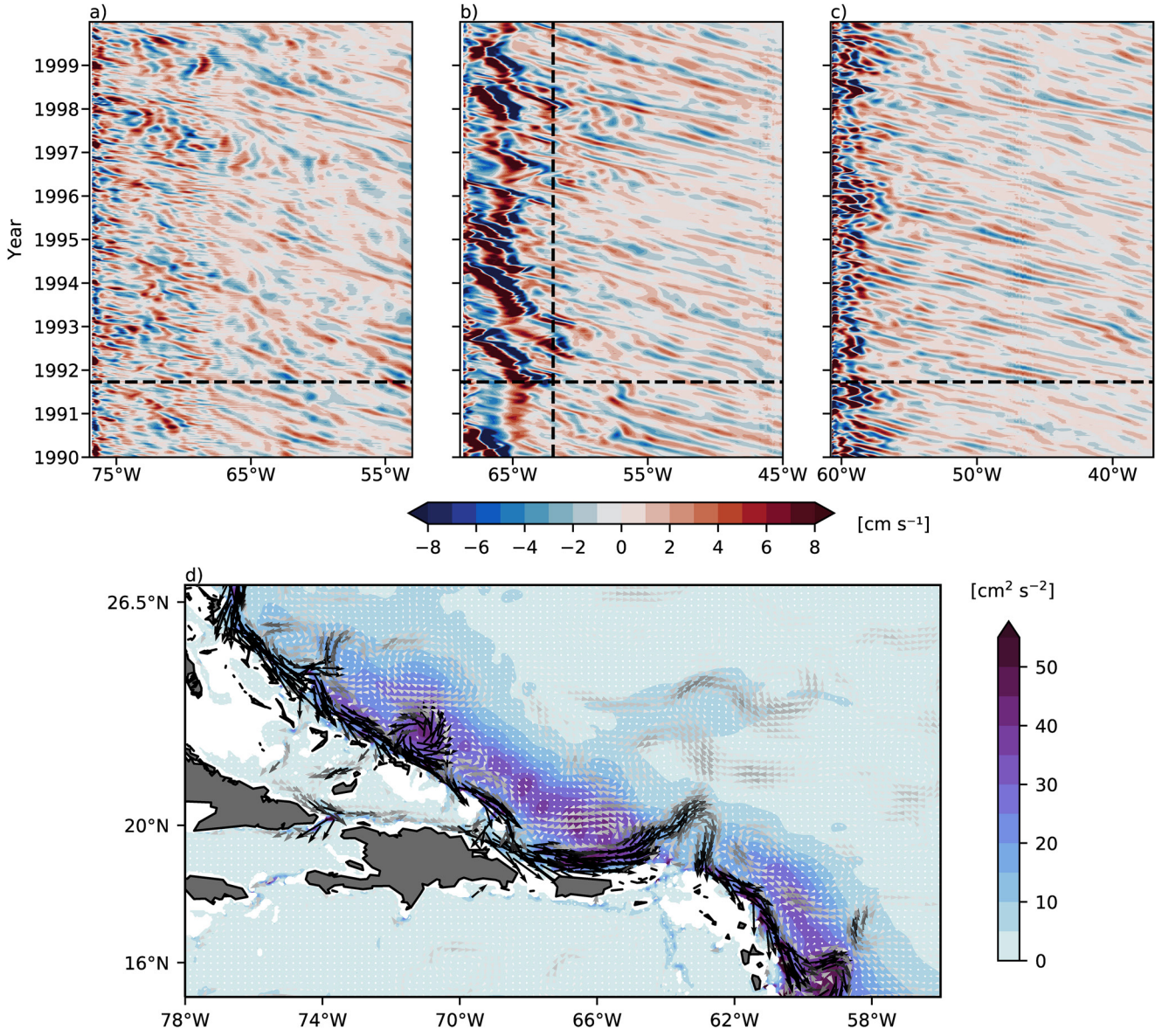

Figure 9. Hovmöller plots of the mean meridional velocity anomaly between 1,000 and 3,500 m depth at 26.5°N (a), 20°N (b) and 16°N (c). The horizontal dashed lines indicate the time step shown in (d). The edge of Lesser Antilles Arc at 20°N is marked with a vertical dashed line. (d) Mean Eddy Kinetic Energy (EKE) (1,000–3,500 m) calculated based on 5-day anomalies from annual means (1990–1999). Vectors show a snapshot (5-day mean) of the velocity field in the same depth range.

both exceeding 8 cm s^{-1} at many time steps. This longitude approximately corresponds to the eastern edge of the Lesser Antilles Arc. Note that the DWBC flows parallel to this section and is located further south. Meridional velocity anomalies west of 60°W are associated with meanders of the DWBC. This can be seen in Figure 9d, where vectors show the 5-day mean velocity field. The positive and negative velocity anomalies associated with the meander centered around 63°W are clearly visible in Figure 9b at the time of the snapshot (horizontal black line). As indicated by the slanting of the anomaly bands to the left, the meander propagates westward (upstream) with a speed around 1.3 cm s^{-1} until the end of 1992. A similar evolution of the flow can be seen for most of the time period shown in Figure 9b. Accordingly, the meander between 68°W and 60°W seen in the LSFs of all Lagrangian experiments is not a steady flow feature, but result of a repeating formation process. Similarly the meridional velocity at 16°N is characterized by strong variability close to the western boundary, showing the frequent existence of eddies at this latitude. At both latitudes, the western boundary regime is clearly separated from the interior ocean. The strong variability along the

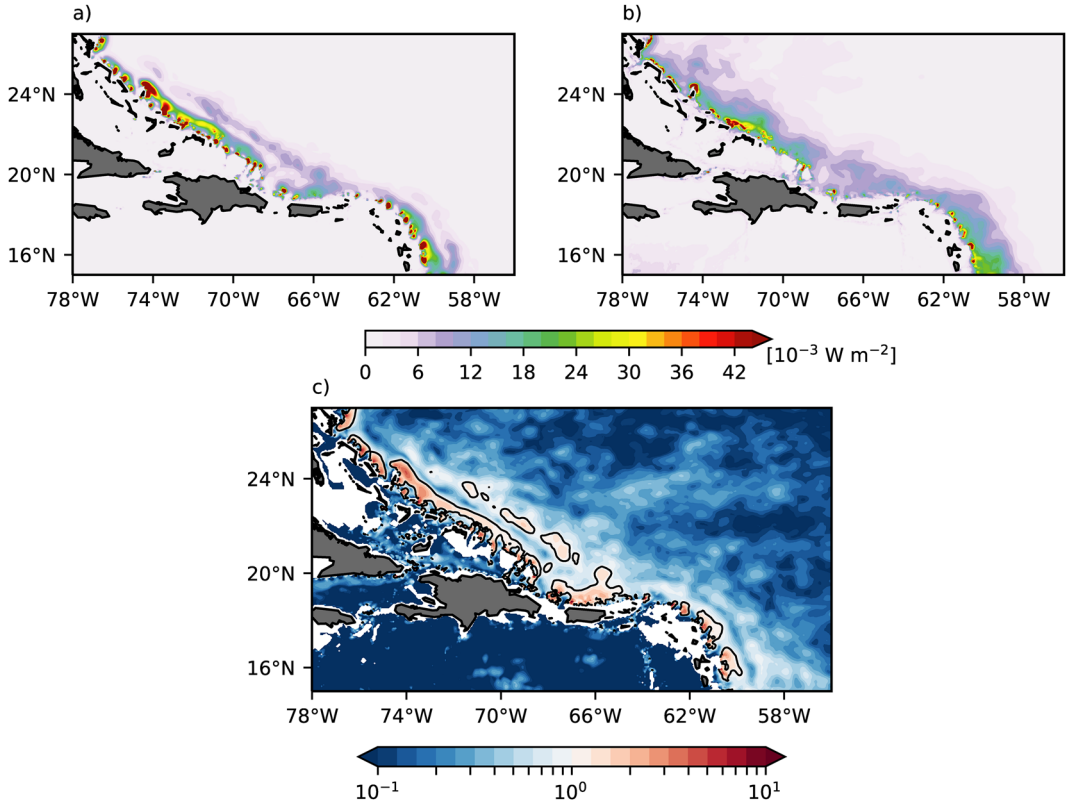

Figure 10. (a) Mean (1990–1999) Barotropic Instability Term $\langle BTI_+ \rangle$ and (b) Baroclinic Instability Term $\langle BCI_+ \rangle$. Both terms are calculated based on 5-day anomalies from annual mean fields and vertically integrated from 1,000 to 3,500 m depth. (c) shows the ratio $\langle BTI_+ \rangle / \langle BCI_+ \rangle$.

western boundary is therefore not directly caused by the arrival of Rossby waves. At 26.5°N this separation is less pronounced. Velocity anomalies are less intensified toward the DWBC. In agreement with Biló and Johns (2020), northward propagating eddies can be seen in the model (Movie S1), but their magnitude is weaker and their occurrence less frequent compared to the eddies and meanders further south. Therefore, the mechanisms driving variability at 26.5°N are different from those at 16°N. This is further supported by the deep EKE in this region (Figure 9d). Along most of the DWBC pathway, EKE is highly elevated compared to the interior ocean. However, north of San Salvador (24°N) EKE values remain low toward the DWBC. Overall, we can conclude that the recirculation gyres seen in the Lagrangian experiments are caused by transient mesoscale features, such as eddies or meanders of the DWBC. The only exception is the cyclonic circulation north of San Salvador that is partly responsible for the return of water to 26.5°N. In line with a description of Leaman and Vertes (1996) and the low EKE values this circulation is stationary.

To gain more information about the generation of eddies south of 24°N, we calculate the positive energy transfers due to barotropic instability (BTI_+) and due to baroclinic instability (BCI_+) following Schubert et al. (2018). Both terms represent local sources of EKE. The $\langle BTI_+ \rangle$ term, with $\langle\ \rangle$ denoting the 10-year average from 1990 to 1999 and vertical integral from 1,000 to 3,500 m, is close to zero in the interior ocean, but strongly enhanced along the western boundary (Figure 10). Especially from San Salvador (24°N) to about 20°N and along the Lesser Antilles Arc (60°W), a high transfer to EKE by barotropic instability can be seen. The baroclinic energy transfer term $\langle BCI_+ \rangle$ shows a similar spacial distribution. However, elevated values are less confined to the western boundary and maximum values are lower compared to $\langle BTI_+ \rangle$. The difference between both terms is more clearly visible in the ratio $\langle BTI_+ \rangle$ / $\langle BCI_+ \rangle$ (Figure 10c). While the interior ocean and Caribbean Sea are dominated by values smaller than one, indicating a dominance of baroclinic instability, the ratio is larger than one along most of the DWBC pathway. Accordingly, barotropic instability caused by a strong horizontal shear at the edge of the DWBC is the main local source of EKE close to the western boundary. Especially south of San Salvador and upstream of the anticyclonic meander

(68°W–60°W) $\langle BTI_+ \rangle$ is about one magnitude larger than $\langle BCI_+ \rangle$. Although Rossby waves are not directly responsible for the variability at the western boundary, they could be an important source of EKE as they reflect into short Rossby waves somewhat caught at the western boundary (Biló & Johns, 2020).

5. Summary and Discussion

In this study, deep flow variability and its implications for the advective spreading of deepwater and the coherence of transport changes at 26.5°N and 16°N were studied. While the AMOC was shown to be highly correlated on interannual to decadal timescales, the correlation of the DWBC transport across both latitudes is not statistically significant. This is in line with the missing impact of advection on coherent variability on annual to interannual timescales north of 38°N (Elipot et al., 2013). In contrast to these latitudes, the importance of slow interior pathways is not a possible explanation for this observation between 26.5°N and 16°N. After being released in the DWBC at 26.5°N, about 20 Sv follow a continuous pathway along the western boundary and reach 16°N. In the following we discuss the sources of temporal variability and differences at the latitudes of 26.5°N and 16°N. Thereafter we address the main questions raised in Section 1 by discussing the impact of mesoscale recirculations on the spreading of deepwater and coherent variability.

5.1. Sources of Temporal Variability in the STNA

The flow to 16°N is subject to strong exchange with the interior ocean caused by temporal variability, in agreement with observations (e.g., Leaman & Vertes, 1996; Rhein et al., 2004). There seems to be an important difference in the mechanism driving temporal variability north and south of San Salvador (24°N). Temporal variability on the northern side is weaker in the model, although this could be a bias of VIKING20X. According to a recent study by Biló and Johns (2020), temporal variability is mainly driven by southward (downstream) propagating meanders and (less frequent) northward propagating eddies, which is in agreement with our results. Temporal variability further south shows different patterns and is associated with southward propagating mesoscale eddies between 24°N and 20°N, and upstream propagating meanders (along the coast of Puerto Rico). At 16°N intense eddies may arrive from the north or south and are present at the vast majority of time steps analyzed here. Although the flow is not steady, a repeating formation process leads to an imprint of these features in the long term averaged velocity field. We find the dominant local source of EKE resulting from barotropic instability of the flow. Consistently, Xu et al. (2012) find mesoscale recirculations in the HYCOM model at very similar locations. Their robustness in both models supports the assumption, that their formation is associated with a strong horizontal shear of the flow at distinct locations. Especially, the Bahamas and Virgin Islands seem to trigger mesoscale recirculations.

5.2. Differences in the Recirculation Across 26.5°N and 16°N

Along with the different mechanisms generating temporal variability, we also find a notable difference between the volume transport recirculations across 26.5°N and 16°N. At 26.5°N the recirculation is supplied by the Abaco Gyre, a persistent cyclonic flow north of San Salvador. Lagrangian studies by Leaman and Vertes (1996) and Riser et al. (1978) show several floats turning north-eastward as they approach 24°N, following similar pathways as indicated by the LSFs shown here. Additionally, water that is detrained from the DWBC by eddies further south adds to the recirculation. A stronger DWBC is likely related to an enhancement through the Abaco Gyre. Also an increase in eddy activity south of San Salvador would be consistent with barotropic instability contributing to their generation. With increasing speed of the DWBC, the horizontal shear gets stronger. This could explain the strong dependence of the return flow on the DWBC strength seen in Section 4.3. Here it is important to consider the impact of a too low EKE at 26.5°N in VIKING20X. Biló and Johns (2020) show that variability on the timescales we consider here is dominated by eddies from south of 24°N. It is not trivial to state how their representation in VIKING20X affects our results. The direct impact of these very infrequent eddies on the volume transport to 26.5°N is likely small, but their reduced magnitude could lead to a stronger connection of the DWBC and Abaco Gyre strength. At 16°N we find the recirculation to be mainly associated with strong mesoscale eddies and there is no persistent recirculation equivalent to the Abaco Gyre. Although eddies can be also seen at 26.5°N they occur more frequently at 16°N, where the connection between DWBC strength and recirculation is weaker. This implies

that the presence of eddies is not directly related to the DWBC strength at 16°N. Extending our study to latitudes further south could show the origin of these eddies and help to understand this observation.

5.3. How does Temporal Variability Affect the Southward Spreading of Deepwater in the STNA?

Temporal variability driven by mesoscale activity in the STNA has a pronounced impact on the volume transport. Together with the nonuniform velocity structure of the DWBC, mesoscale recirculations contribute to the spread between tracer-based and current-meter estimates of the southward velocity in this region. Even long-term averages of the Eulerian velocity can exceed 30 cm s^{-1} in the DWBC core. The speed associated with the Lagrangian mean transit time is 5 cm s^{-1} in EXP_{mn}, mainly reflecting that not all the water that reaches 16°N is transported in the DWBC core, where velocities are highest. Adding recirculations further reduces the mean speed to 4 cm s^{-1}. This spread has important implications by extending the timelag of tracer concentration changes at remote locations and increasing the residence time of anthropogenic carbon dioxide in the deep ocean. Additionally, stirring by mesoscale eddies mixes tracers transported in the DWBC into the interior ocean in agreement with Rhein et al. (2004).

5.4. Can Advection in the DWBC Cause Coherent AMOC Changes in the STNA?

The recirculations lead to a decorrelation of the transport signals at 26.5°N and 16°N. Note that we only study the advective part of the signal propagation, so that decorrelation only refers to the advective component. Boundary waves and wind forcing as different processes to drive coherent changes are not taken into question. Based on our study of the DWBC's timescale these processes are clearly distinguishable based on the expected timelag (being much shorter for wave adjustment) and therefore do not interfere with our results. Recirculations are responsible for a northward return flow to 26.5°N. Bryden et al. (2005) derive a northward recirculation of 13 Sv, which matches our Lagrangian estimate of 10 Sv and shows that most of the northward flow in the vicinity of the western boundary is supplied by water detrained from the DWBC. The strength of the return flow is higher correlated with the DWBC than the component that reaches the MOVE section. Accordingly, additional water volumes associated with an above average DWBC transport are mostly returned to 26.5°N. As a result, the correlation between the DWBC transport and the transport that reaches 16°N is 0.55. Along the pathway to 16°N the transport signal is altered by a broad and variable TTD. The pure broadening of the TTD lengthens the advective timescale and shifts the maximum cross-correlation of the transport signal at release and arrival to longer transit times. However, the impact on the maximum correlation itself is small. In contrast, the correlation decreases when the temporal variability of the TTD itself is considered. Not only the added variety of pathways, but also the fact that trajectories released at different time steps will take different routes, reduces the correlation. This has important implications for observational studies using Lagrangian techniques. A TTD derived from a single float release (or very few release times) must not represent the mean distribution even without considering uncertainties from a limited spatial coverage of the DWBC. This also shows the importance of releasing virtual particles/water volumes over a time period as long as possible in modeling studies. To estimate the variability of the TTD is especially important when a study aims to infer changes of a signal along the pathway. As EKE in VIKING20X is lower than in observations at 26.5°N, the TTD may be even more variable and changes of the signal along the pathway even stronger in the real ocean. At 16°N the correlation of the transport arriving from 26.5°N and the DWBC at 26.5°N is already statistically insignificant. Additionally, the DWBC at 16°N is not fully supplied by water advected in the DWBC from 26.5°N. A local recirculation of 7 Sv further decouples the DWBC transport at both latitudes. As a consequence, advection in the DWBC does not play a role for the coherence of AMOC changes on interannual timescales, even though it is responsible for a strong mean flow between the latitudes with a timescale well below 2 years. Consistent with this result, the strong AMOC correlation is found at timelag zero without any significant peaks at timelags corresponding to the advective timescale. This may not be surprising based on modeling studies finding AMOC anomalies to propagate with Kelvin wave speed (Getzlaff et al., 2005; Zhang, 2010). Still the missing impact of advection on interannual timescales is not trivial, especially in the latitude range studied here. Our study provides information about mechanisms that decouple transport variations at remote sections, despite the existence of a strong, continuous mean current connecting them. Further, the existence of highly variable recirculations stresses the importance of trans-basin AMOC measurements. The southward DWBC transport does

not provide a good estimate of the total southward transport across the section. It is also not possible to simply include the recirculation to calculate a mean southward transport. Especially at 26.5°N the recirculation is rather broad with a variable extend and not connected to a clear maximum of the cumulative deep transport (from west to east) at many time steps. Note however, that the long term mean Lagrangian transport to the MOVE section (19.3 Sv) matches the mean AMOC of about 19 Sv in the STNA. This confirms that the main NADW pathway in this region is the DWBC.

Overall, our results are consistent with the conclusion of Frajka-Williams et al. (2018) that the different trends observed at MOVE and RAPID between 2004 and 2015 are caused by differences in the methodology of the transport calculation, not an actual difference in the transport tendency. First, the 119-months low-pass filtered AMOC timeseries in the model show a correlation of 0.95. As a result, different trends within a time span of around 10-years (filtering period), are not existent in the model. Second, our results suggest that the decorrelation of the (advective) transport signals at 16°N and 26.5°N is almost negligible on decadal timescales. Advection could therefore play an important role for the coherent, basin wide AMOC adjustment on decadal timescales described by Biastoch et al. (2008). However, our Lagrangian experiments only cover 30 years and are too short for robust results on this timescale. On interannual (and shorter) timescales, on the other hand, opposing anomalies are possible. At least advection in the DWBC does not determine the AMOC to show similar changes at 26.5°N and 16°N. This is apparent in the lower correlation of 0.57 for the 23-month low-pass filtered timeseries in the model. Nevertheless, this correlation is still significantly different from zero in agreement with Bingham et al. (2007). But instead of advection in the DWBC, wind forcing seems to be the driver of coherent interannual changes at MOVE and RAPID. Biastoch et al. (2008) and Zhao and Johns (2014) find interannual AMOC variations to be dominated by wind forcing in the STNA. Further, Elipot et al (2016) report on coherent changes across the STNA driven by a NAO-type wind pattern. Although the RAPID timeseries shows an inconsistent overturning response to this pattern compared to MOVE, Line W (39.8°N) and WAVE (42.58°N), this may only result from the very limited length of their timeseries. Here we took a first step in understanding processes that can impact the coherence of AMOC changes at remote locations. A detailed study of coherence driven by wind patterns or boundary waves is left for further research.

Data Availability Statement

Model computations and data analysis were performed at the North German Supercomputing Alliance (HLRN). The data is available at https://hdl.handle.net/20.500.12085/ec430a5c-1930-4a87-bb1f-973162c2a135. The MOVE transport time series used for model validation is available at http://www.oceansites.org/tma/move.html.

Acknowledgments
The study was supported by the cooperative program "RACE-Regional Atlantic Circulation and Global Change" (BMBF Grant 03F0729C) and the European Union's Horizon 2020 research and innovation programme under grant agreement No 818123 (iAtlantic).

References

Barnier, B., Madec, G., Penduff, T., Molines, J.-M., Treguier, A.-M., Le Sommer, J., & Cuevas, B. (2006). Impact of partial steps and momentum advection schemes in a global ocean circulation model at eddy-permitting resolution. *Ocean Dynamics*, *56*(5), 543–567. https://doi.org/10.1007/s10236-006-0082-1

Biastoch, A., Böning, C. W., Getzlaff, J., Molines, J.-M., & Madec, G. (2008). Causes of interannual-decadal variability in the meridional overturning circulation of the midlatitude North Atlantic Ocean. *Journal of Climate*, *21*(24), 6599–6615. https://doi.org/10.1175/2008JCLI2404.1

Biastoch, A., Schwarzkopf, F. U., Getzlaff, K., Rühs, S., Martin, T., Scheinert, M., et al. (2021). Regional imprints of changes in the Atlantic meridional overturning circulation in the eddy-rich ocean model VIKING20X. *Ocean Science*, 1–52. https://doi.org/10.5194/os-2021-37

Biló, T. C., & Johns, W. E. (2020). The deep western boundary current and adjacent interior circulation at 24°-30°N: Mean structure and mesoscale variability. *Journal of Physical Oceanography*, *50*(9), 2735–2758. https://doi.org/10.1175/JPO-D-20-0094.1

Bingham, R. J., Hughes, C. W., Roussenov, V., & Williams, R. G. (2007). Meridional coherence of the North Atlantic meridional overturning circulation. *Geophysical Research Letters*, *34*, L23606. https://doi.org/10.1029/2007GL031731

Blanke, B., Arhan, M., Madec, G., & Roche, S. (1999). Warm water paths in the equatorial Atlantic as diagnosed with a general circulation model. *Journal of Physical Oceanography*, *29*(11), 2753–2768. https://doi.org/10.1175/1520-0485(1999)029<2753:wwpite>2.0.co;2

Blanke, B., & Raynaud, S. (1997). Kinematics of the pacific equatorial undercurrent: An Eulerian and Lagrangian approach from GCM Results. *Journal of Physical Oceanography*, *27*(6), 1038–1053. https://doi.org/10.1175/1520-0485(1997)027<1038:kotpeu>2.0.co;2

Böning, C. W., Behrens, E., Biastoch, A., Getzlaff, K., & Bamber, J. L. (2016). Emerging impact of Greenland meltwater on deepwater formation in the North Atlantic Ocean. *Nature Geoscience*, *9*(7), 523–527. https://doi.org/10.1038/ngeo2740

Bower, A. S., Lozier, M. S., Gary, S. F., & Böning, C. W. (2009). Interior pathways of the North Atlantic meridional overturning circulation. *Nature*, *459*(7244), 243–247. https://doi.org/10.1038/nature07979

Bryden, H. L., Johns, W. E., & Saunders, P. M. (2005). Deep western boundary current east of Abaco: Mean structure and transport. *Journal of Marine Research*, *63*(1), 35–57. https://doi.org/10.1357/0022240053693806

Debreu, L., Vouland, C., & Blayo, E. (2008). AGRIF: Adaptive grid refinement in Fortran. *Computers & Geosciences*, *34*(1), 8–13. https://doi.org/10.1016/j.cageo.2007.01.009

Delandmeter, P., & van Sebille, E. (2019). The parcels v2.0 lagrangian framework: New field interpolation schemes. *Geoscientific Model Development*, *12*(8), 3571–3584. https://doi.org/10.5194/gmd-12-3571-2019

Elipot, S., Frajka-Williams, E., Hughes, C. W., Olhede, S., & Lankhorst, M. (2016). Observed basin-scale response of the North Atlantic meridional overturning circulation to wind stress forcing. *Journal of Climate*, *30*(6), 2029–2054. https://doi.org/10.1175/JCLI-D-16-0664.1

Elipot, S., Hughes, C., Olhede, S., & Toole, J. (2013). Coherence of western boundary pressure at the RAPID WAVE array: Boundary wave adjustments or deep western boundary current advection? *Journal of Physical Oceanography*, *43*(4), 744–765. https://doi.org/10.1175/JPO-D-12-067.1

Emery, W. J., & Thomson, R. E. (2001). Time-series analysis methods. In W. J. Emery & R. E. Thomson (Eds.), *Data analysis methods in physical oceanography* (pp. 371–567). Amsterdam. Elsevier Science. https://doi.org/10.1016/B978-044450756-3/50006-X

Frajka-Williams, E., Lankhorst, M., Koelling, J., & Send, U. (2018). Coherent circulation changes in the deep North Atlantic from 16°N and 26°N transport arrays. *Journal of Geophysical Research: Oceans*, *123*, 3427–3443. https://doi.org/10.1029/2018JC013949

Gary, S. F., Susan Lozier, M., Böning, C. W., & Biastoch, A. (2011). Deciphering the pathways for the deep limb of the meridional overturning circulation. *Deep Sea Research Part II: Topical Studies in Oceanography*, *58*(17–18), 1781–1797. https://doi.org/10.1016/j.dsr2.2010.10.059

Getzlaff, J., Böning, C. W., Eden, C., & Biastoch, A. (2005). Signal propagation related to the North Atlantic overturning. *Geophysical Research Letters*, *32*, L09602. https://doi.org/10.1029/2004GL021002

Gill, A. (1982). *Atmosphere-ocean dynamics* (1st ed). New York. Academic Press.

Johns, W. E., Kanzow, T., & Zantopp, R. (2005). Estimating ocean transports with dynamic height moorings: An application in the Atlantic deep western boundary current at 26°N. *Deep Sea Research Part I: Oceanographic Research Papers*, *52*(8), 1542–1567. https://doi.org/10.1016/j.dsr.2005.02.002

Kanzow, T., Send, U., & McCartney, M. (2008). On the variability of the deep meridional transports in the tropical North Atlantic. *Deep Sea Research Part I: Oceanographic Research Papers*, *55*(12), 1601–1623. https://doi.org/10.1016/j.dsr.2008.07.011

Kanzow, T., Send, U., Zenk, W., Chave, A. D., & Rhein, M. (2006). Monitoring the integrated deep meridional flow in the tropical North Atlantic: Long-term performance of a geostrophic array. *Deep Sea Research Part I: Oceanographic Research Papers*, *53*(3), 528–546. https://doi.org/10.1016/j.dsr.2005.12.007

Large, W. G., & Yeager, S. G. (2009). The global climatology of an interannually varying air-sea flux data set. *Climate Dynamics*, *33*(2), 341–364. https://doi.org/10.1007/s00382-008-0441-3

Leaman, K. D., & Vertes, P. S. (1996). Topographic influences on recirculation in the deep western boundary current: Results from RAFOS float trajectories between the Blake-Bahama outer ridge and the San Salvador "Gate". *Journal of Physical Oceanography*, *26*(6), 941–961. https://doi.org/10.1175/1520-0485(1996)026<0941:tiorit>2.0.co;2

Lee, T. N., Johns, W., Zantopp, R., & Schott, F. (1990). Western boundary current structure and variability east of Abaco, Bahamas at 26.5°N. *Journal of Physical Oceanography*, *20*(3), 446–466. https://doi.org/10.1175/1520-0485(1990)020<0446:wbcsav>2.0.co;2

Lee, T. N., Johns, W. E., Zantopp, R. J., & Fillenbaum, E. R. (1996). Moored observations of western boundary current variability and thermohaline circulation at 26.5° in the subtropical North Atlantic. *Journal of Physical Oceanography*, *26*(6), 962–983. https://doi.org/10.1175/1520-0485(1996)026<0962:moowbc>2.0.co;2

Lüschow, V., Storch, J.-S. V., & Marotzke, J. (2019). Diagnosing the influence of mesoscale eddy fluxes on the deep western boundary current in the 1/10° STORM/NCEP simulation. *Journal of Physical Oceanography*, *49*(3), 751–764. https://doi.org/10.1175/JPO-D-18-0103.1

Madec, G. (2016). *Nemo ocean engine. Note du Pôle de modélisation*, France. Institut Pierre-Simon Laplace (IPSL). No 27, ISSN No 1288-1619

Pickart, R. S., Hogg, N. G., & Smethie, W. M. (1989). Determining the strength of the deep western boundary current using the chlorofluoromethane ratio. *Journal of Physical Oceanography*, *19*(7), 940–951. https://doi.org/10.1175/1520-0485(1989)019<0940:dtsotd>2.0.co;2

Rhein, M. (1994). The deep western boundary current: Tracers and velocities. *Deep Sea Research Part I: Oceanographic Research Papers*, *41*(2), 263–281. https://doi.org/10.1016/0967-0637(94)90003-5

Rhein, M., Kieke, D., & Steinfeldt, R. (2015). Advection of North Atlantic deep water from the Labrador Sea to the southern hemisphere. *Journal of Geophysical Research: Oceans*, *120*, 2471–2487. https://doi.org/10.1002/2014JC010605

Rhein, M., Walter, M., Mertens, C., Steinfeldt, R., & Kieke, D. (2004). The circulation of North Atlantic deep water at 16°N, 2000-2003. *Geophysical Research Letters*, *31*, L14305. https://doi.org/10.1029/2004GL019993

Rieck, J. K., Böning, C. W., & Getzlaff, K. (2019). The nature of eddy kinetic energy in the Labrador Sea: Different types of mesoscale eddies, their temporal variability, and impact on deep convection. *Journal of Physical Oceanography*, *49*(8), 2075–2094. https://doi.org/10.1175/JPO-D-18-0243.1

Riser, S. C., Freeland, H., & Rossby, H. T. (1978). Mesoscale motions near the deep western boundary of the North Atlantic. *Deep Sea Research*, *25*(12), 1179–1191. https://doi.org/10.1016/0146-6291(78)90012-7

Rühs, S., Schwarzkopf, F. U., Speich, S., & Biastoch, A. (2019). Cold vs. warm water route - Sources for the upper limb of the Atlantic meridional overturning circulation revisited in a high-resolution ocean model. *Ocean Science*, *15*(3), 489–512. https://doi.org/10.5194/os-15-489-2019

Sabine, C. L., Feely, R. A., Gruber, N., Key, R. M., Lee, K., Bullister, J. L., & Rios, A. F. (2004). The oceanic sink for anthropogenic CO_2. *Science*, *305*(5682), 367–371. https://doi.org/10.1126/science.1097403

Schubert, R., Biastoch, A., Cronin, M. F., & Greatbatch, R. J. (2018). Instability-driven benthic storms below the separated gulf stream and the North Atlantic Current in a high-resolution ocean model. *Journal of Physical Oceanography*, *48*(10), 2283–2303. https://doi.org/10.1175/JPO-D-17-0261.1

Send, U., Lankhorst, M., & Kanzow, T. (2011). Observation of decadal change in the Atlantic meridional overturning circulation using 10 years of continuous transport data. *Geophysical Research Letters*, *38*, L24606. https://doi.org/10.1029/2011GL049801

Smeed, D. A., McCarthy, G. D., Cunningham, S. A., Frajka-Williams, E., Rayner, D., Johns, W. E., et al. (2014). Observed decline of the Atlantic meridional overturning circulation 2004-2012. *Ocean Science*, *10*(1), 29–38. https://doi.org/10.5194/os-10-29-2014

Srokosz, M. A., & Bryden, H. L. (2015). Observing the Atlantic meridional overturning circulation yields a decade of inevitable surprises. *Science*, *348*(6241), 1255575. https://doi.org/10.1126/science.1255575

van Sebille, E., Griffies, S. M., Abernathey, R., Adams, T. P., Berloff, P., Biastoch, A., et al. (2018). Lagrangian ocean analysis: Fundamentals and practices. *Ocean Modelling*, *121*, 49–75. https://doi.org/10.1016/j.ocemod.2017.11.008

Waugh, D. W., & Hall, T. M. (2005). Propagation of Tracer signals in boundary currents. *Journal of Physical Oceanography*, *35*(9), 1538–1552. https://doi.org/10.1175/JPO2779.1

Xu, X., Schmitz, W. J., Jr, Hurlburt, H. E., & Hogan, P. J. (2012). Mean Atlantic meridional overturning circulation across 26.5°N from eddy-resolving simulations compared to observations. *Journal of Geophysical Research*, *117*, C03042. https://doi.org/10.1029/2011JC007586

Zhang, R. (2010). Latitudinal dependence of Atlantic meridional overturning circulation (AMOC) variations. *Geophysical Research Letters*, *37*, L16703. https://doi.org/10.1029/2010GL044474

Zhao, J., & Johns, W. (2014). Wind-forced interannual variability of the Atlantic meridional overturning circulation at 26.5°N. *Journal of Geophysical Research: Oceans*, *119*, 2403–2419. https://doi.org/10.1002/2013JC009407